



सिरामिक अभियांत्रिकी विभाग

Phone: +91-542-6701787

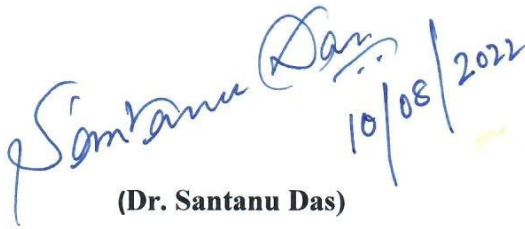
DEPARTMENT OF CERAMIC ENGINEERING

Fax: +91-542-2368428 Email: head.cer@itbhu.ac.in

Date: 10/08/2022

CERTIFICATE

This is to certify that the thesis entitled “*Development of Two-dimensional Functional Nanostructures for Electrocatalysis and Photocatalysis*” being submitted by **Vivek Kumar Singh (Roll No- 18031006)** to the Indian Institute of Technology (Banaras Hindu University) Varanasi, for the award of the Degree of Doctor of Philosophy in the Department of Ceramic Engineering is a record of bonafide research work carried out absolutely by him under our supervision and guidance. The thesis has reached the standard; fulfilling the requirements of the regulations relating to the nature of the degree. The results embodied in this thesis have not been submitted to any other university or institute for the award of any degree or diploma.


(Dr. Santanu Das)

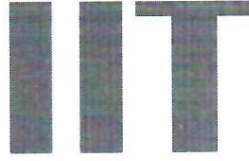
Supervisor

Dr. SANTANU DAS/डा० शान्तनु दास
Assistant Professor/असिस्टेंट प्रोफेसर
Department of Ceramic Engg./सिरामिक इंजिनियरिंग विभाग
Indian Institute of Technology (BHU)/भारतीय प्रौद्योगिकी संस्थान वी.एच.यू.
Varanasi-221005, U.P., India/वाराणसी-२२१००५, उ०प्र०, भारत.


Head of the Department
HEAD/विभागाध्यक्ष
Department of Ceramic Engineering
सिरामिक अभियांत्रिकी विभाग
Indian Institute of Technology (B.H.U.)
भारतीय प्रौद्योगिकी संस्थान (का०हि०वि०पि०)
Varanasi-221005/ वाराणसी- 221005



भारतीय
प्रौद्योगिकी
संस्थान
काशी हिन्दू विश्वविद्यालय



INDIAN
INSTITUTE OF
TECHNOLOGY
BANARAS HINDU UNIVERSITY

सिरामिक अभियांत्रिकी विभाग

Phone: +91-542-6701787

DEPARTMENT OF CERAMIC ENGINEERING

Fax: +91-542-2368428 Email: head.cer@itbhu.ac.in

Date: 10/08/2022

CANDIDATE'S DECLARATION

*I hereby declare that the work presented in the dissertation entitled "**Development of Two-dimensional Functional Nanostructures for Electrocatalysis and Photocatalysis**" is an authentic record of my own work carried out at the Department of Ceramic Engineering, Indian Institute of Technology (Banaras Hindu University), Varanasi as the requirement for the award of the degree of doctor of philosophy in Ceramic Engineering, submitted in the Indian Institute of Technology (Banaras Hindu University), Varanasi for the session 2018-19 under the supervision of **Dr. Santanu Das**, Department of Ceramic Engineering Indian Institute of Technology (Banaras Hindu University), Varanasi.*

It does not contain any part of the work, which has been submitted for the award of any degree either in this university or in the other university/Deemed University without proper citation.

Vivek Kumar Singh
10/08/2022

Mr. Vivek Kumar Singh

Roll No. 18031006

Department of Ceramic Engineering,
IIT(BHU), Varanasi

COPYRIGHT TRANSFER CERTIFICATE

Title of the Thesis: **Development of Two-dimensional Functional Nanostructures for Electrocatalysis and Photocatalysis**

Name of the Student: **Vivek Kumar Singh**

Copyright Transfer

The undersigned hereby assigns to the Indian Institute of Technology (Banaras Hindu University), Varanasi all rights under copyright that may exist in and for the above thesis submitted for the award of the Doctor of Philosophy.

Date: 10/08/2022


Signature of the Student

Place: IIT-BHU
Varanasi

Vivek Kumar Singh

Note: However, the author may reproduce or authorize others to reproduce material extracted verbatim from the thesis or derivative of the thesis for author's personal use provided that the source and the Institute's copyright notice are indicated.

Acknowledgment

This dissertation is the culmination of my PhD experience, which was akin to ascending a treacherous mountain all the while encountering encouragement, struggle, bitterness, frustration, and faith and it gives me immense pleasure to take this opportunity to offer my heartfelt gratitude to everyone who contributed to this thesis and assisted me along this incredible journey of my PhD.

I would like to take this opportunity to convey my heartfelt gratitude to Dr. Santanu Das, my PhD supervisor for accepting me as his student and giving me an insight and an understanding of the research world. He has always been patient and encouraging me, while discussing new ideas and guiding me towards the right direction. This research would not have been possible without his invaluable guidance.

I am deeply indebted to the members of my research performance evaluation committee (RPEC), Dr. Bhola Nath Pal, School of Materials Science and Technology, and Dr. Imteyaz Ahmad, Department of Ceramic Engineering whose suggestions and critical comments during my semester progress presentations contributed immensely in refining and moulding my thesis.

I would also like to thank Dr. Bratindranath Mukherjee, Department of Metallurgical Engineering, IIT (BHU), Varanasi, for helping me all the way throughout my PhD research.

I also express my heartfelt thanks to Dr. S. Assa Aravindh, University of Oulu, Finland for collaborating and analysing DFT Calculations and Simulations.

I also acknowledge the Department of Science and Technology, Government of India for providing financial support (Grant No: DST/INSPIRE Fellowship/2017/IF170977) throughout my PhD journey.

A thank from the bottom of my heart goes to the Head of the Department of Ceramic Engineering, IIT (BHU), Varanasi for providing me all the facilities to conduct my research

work. I would also like to thank all the faculty members, laboratory staff, librarians, and office staff for their kind cooperation and encouragement during this incredible journey.

Thanks to Central Instrument Facility (CIF), IIT (BHU) for the support for various state-of-the-art characterizations and all the research collaborators in India and Worldwide for collaborating with us and extending their support throughout my PhD tenure.

I am grateful to my colleagues in the Nanomaterials for Electronics and energy Devices (NEED) Lab for their constant help and never-ending efforts to make the lab an enthusiastic place for research and learning. Specifically, my heartfelt thanks go to Mr. Sabyasachi Roy, Mr. Uttam Sharma, Ms. Ummya Qamar, Mr. Sayak Roy, Mr. Sayan Chattopadhyay, Ms. Prachi Jain, for their constant helps and supports during my Ph.D. period.

My thanks and sincere appreciation also go to my friends, especially Mr. Kunal Verma, Mr. Siddharth Singh, Mr. Taranga Dehury, Mr. Manish Chourasia, Mr. Supriya Chanda, Mr. Rakesh Kumar, Mr. Aman Singh, Mr. Amit Sharma, Mr. Amit Kumar Singh, Mr. Manas Ranjan Samantaray, Mr. Abhay Kumar Mondal, Mr. Satyendra Kumar Singh, Mr. Vaibhav Singh, Mr. Vaibhav Panday, Mr. Ramakant Kumar for their constant support.

I would like to express my heartfelt gratitude to my beloved parents Shri. Vijay Bahadur Singh and Smt. Punam Singh for their constant support and love throughout my life.

My appreciation toward my brother Mr. Vishal Kumar Singh and my sister Pooja Singh for their continuous support and encouragement.

Above all, I thank Lord Vishwanath for providing me with strength and courage in completing the work.

Sincerely,

Vivek Kumar Singh

**THIS THESIS IS DEDICATED TO MY
PARENTS**

CONTENTS		Page No.
<i>List of Figures</i>		XIII-XXII
<i>List of Tables</i>		XXIII
<i>List of Abbreviations</i>		XXIV-XXVI
Chapter 1: Introduction and Literature Survey		2-58
1.1	Introduction	2
	1.1 An overview of future renewable energy demand	2-4
1.2	Electrochemistry of the hydrogen evolution reaction	4-6
1.3	Fundamentals of hydrogen evolution reaction	6-9
	1.3.1 Reaction mechanism	6-8
	1.3.2. Volcano plots	8-9
1.4	Experimental method for characterizing the electrochemical activity of HER catalysts	9-13
	1.4.1. Overpotential	9-11
	1.4.2. Tafel plot	11-12
	1.4.3. Electrochemical impedance spectroscopy	12
	1.4.4. Stability	12-13
1.5	An overview of the elements used for constructing HER electrocatalysts	13-14
1.6	Two-dimensional functional nanostructures	15-21
	1.6.1 Graphene	16-18
	1.6.2. Two-dimensional transition metal dichalcogenides (TMDs)	18-21
	1.6.2.1 Molybdenum disulfide (MoS ₂)	19-21

1.7	Strategies for improving the catalytic activity of 2H-MoS ₂	21-36
	1.7.1 Increasing edge sites of 2H-MoS ₂	22-24
	1.7.2 Engineering defects in 2H-MoS ₂ and the effect of strain	24-26
	1.7.3 Constructions of heterostructures	26-29
	1.7.4 Heteroatom doping	29-32
	1.7.5 Phase transformation in MoS ₂	33-36
1.8	A novel hierarchical MoNi ₄ /MoO ₂ nanostructures	36-38
1.9	Objectives of this work	38-39
	References	39-58
Chapter 2: Materials and Methods		60-84
2.1	Introduction	60
	2.1.1 Hydrothermal synthesis (HTS)	61
	2.1.2 Synthesis of MoNi ₄ /MoO ₂ nanorods	62
	2.1.3 Graphene oxide (GO) synthesis via modified Hummers' method	63-64
	2.1.4 Synthesis of reduced graphene oxide (rGO)	64
	2.1.5 MoNi ₄ /MoO ₂ :rGO of nanocomposite synthesis	64-65
	2.1.6 Synthesis of 2D-MoS ₂ nanosheets via hydrothermal method	65-66
	2.1.7 Synthesis of MoS ₂ :MoNi ₄ /MoO ₂ nanohybrids	66-67
	2.1.8 Synthesis of sulfonic acid (SO ₃ H) functionalized 2D-MoS ₂ nanosheets	67-68

	2.1.9 Sulfonic acid/ Sulfur trioxide (SO ₃ H/SO ₃) functionalization in 2D-MoS ₂ nanosheets	68-69
2.2	Techniques of materials characterizations	69-78
	2.2.1 X-ray powder diffraction (XRD)	69-70
	2.2.2 Scanning electron microscopy (SEM)	70-71
	2.2.3 Transmission electron microscopy (TEM)	71-72
	2.2.4. X-ray photoelectron spectroscopy (XPS)	72-73
	2.2.5 Raman spectroscopy	74
	2.2.6 Fourier transform infrared spectroscopy (FTIR)	74-75
	2.2.7 Differential scanning calorimetry and thermogravimetric analysis	75
	2.2.8 Ultraviolet-visible spectroscopy (UV-Vis)	76
	2.2.9 Brunauer-Emmett-Teller (BET)	77
	2.2.10 Contact angle measurement	77
2.3	Electrochemical measurements	78-83
	2.3.1 Electrode fabrication	78
	2.3.2 Electrochemical characterizations	79-83
	2.3.2.1 Linear sweep voltammetry (LSV)	80
	2.3.2.2 Electrochemical impedance spectroscopy (EIS)	81-82
	2.3.2.3 Stability	82
	2.3.2.4 Cyclic voltammetry (CV)	82-83
	2.3.2.5 Mott-Schottky (M-S)	83
	References	83-84

Chapter 3: Reduced Graphene Oxide supported MoNi ₄ /MoO ₂ Nanorods for Hydrogen Evolution Reaction		86-104
3.1	Introduction	86-88
3.2	Results and Discussions	88-99
3.3	Chapter Summary	99
	References	100-104
Chapter 4: Two-dimensional (2D) MoS ₂ Nanosheets on MoNi ₄ /MoO ₂ Nanorods for Hydrogen Evolution Reaction		106-136
4.1	Introduction	106-108
4.2	Results and discussions	108-129
4.3	Chapter summary	129-130
	References	130-136
Chapter 5: Functionalized 2D-MoS ₂ Nanosheets for Electrocatalytic Hydrogen Evolution Reaction via Water Electrolysis		138-182
5.1	Introduction	138-141
5.2	Results and discussions	141-166
5.3	Computational methodology	166-171
5.4	Chapter summary	171-172
	References	172-182
Chapter 6: [SO ₃ H/SO ₃] Functionalized 2D-MoS ₂ Nanosheets for Photocatalysis of Organic Pollutants		184-207
6.1	Introduction	184-186
6.2	Results and discussions	186-199

6.3	Chapter summary	199-200
	References	200-207
Chapter 7: Conclusions and Future Scope		209-214
7.1	Conclusions	209-212
7.2	Future scope of work	213-214
Publications, Patents, and Conference Presentations		216-219

LIST OF FIGURES		
Figure 1.1:	Illustration of the hydrogen-based systems and assemblies for supplying energies in future.	4
Figure 1.2:	Demonstrates a typical water electrolysis process; H ₂ and O ₂ are produced at the cathode and anode sides, respectively.	5
Figure 1.3:	Schematic illustration of hydrogen evaluation pathways in acidic (left) and alkaline (right) conditions.	7
Figure 1.4:	(a) Relationship between j_0 and ΔG_{H^*} under the assumption of a Langmuir adsorption model; (b) Dependence of j_0 on ΔG_{H^*} for HER on the surface of various noble metals and non-noble metals in an acidic medium.	9
Figure 1.5:	(a) Schematic showing HER polarization curves of electrocatalysts designated with “iR” drop compensation and overpotential values; (b) schematic demonstration of Tafel plots on other electrocatalysts with the Tafel slopes and exchanges current densities indicated.	11
Figure 1.6:	Shows the periodic table with highlighted elements, which are used for constructing HER catalysts.	13
Figure 1.7:	Illustrates (a) two dimensional atomically thin single-layer graphene is the mother of all the carbon allotropes, such as, fullerene (b); carbon nanotube (c); and graphite (d).	17
Figure 1.8:	Schematic showing (a) key properties of graphene and graphene-based materials for their applications in energy-related devices; (b) the various energy-related applications of graphene.	18
Figure 1.9:	Shows various phases of MoS ₂ unit cells consist of metal coordination and stacking sequences. The way metals are put together can be octahedral or trigonal prismatic. The octahedral coordination makes it possible to stack sequences, which leads to tetragonal symmetry (1T). When trigonal prismatic single layers are stacked in different ways, they can create two different symmetries: hexagonal symmetry (2H) and rhombohedral symmetry (3R).	20
Figure 1.10:	(a) Calculated free energy diagram of HER for various electrocatalysts, including MoS ₂ (0.08 eV) and different metal electrodes such as Au, Pt, Ni, and Mo at pH=0; (b) exchange current density with MoS ₂ as the function of MoS ₂ edge length.	21
Figure 1.11:	(a) Scheme for the synthesis of mesoporous MoS ₂ on double-gyroid engineering to maximally expose edge sites of MoS ₂ for enhanced HER catalytic activity; (b) Edge terminated MoS ₂ film	23

	with maximally exposing the edges of MoS ₂ layers and corresponding HRTEM image; (c) Vertically aligned, step-edge terminated MoS ₂ thin-film and corresponding TEM images.	
Figure 1.12:	Shows (a) schematic representation of defect-free and defect-reach MoS ₂ nanosheets, (b) atomic reconcentration of defect-reach MoS ₂ nanosheets with additional active sites, (c) polarization curve of different MoS ₂ structures where the defect-reach MoS ₂ shows the higher current density; (d) schematic showing the strain-induced S-vacancies on the basal plane of 2D-MoS ₂ , where sulfur-vacancies act as the active sites for HER and applied strain further tunes the HER activity; (e) Free energy versus the reaction coordinate of HER for the sulfur-vacancy range from 0 to 25%; (f) ΔG_H vs. % x-strain for various S-vacancy % from 0 to 18.75%. and (g) polarization curve for the Pt electrode, Au substrate, pristine MoS ₂ (S-vacancy:0% and strain: 0%) strained (S-MoS ₂) MoS ₂ without S-vacancies (S-vacancy:0% and strain: 1.5%), S-vacancy reach (V-MoS ₂) MoS ₂ (S-vacancy:12.5% and strain: 0%) and S-vacancies with strained (SV-MoS ₂) MoS ₂ (S-vacancy 12.5 % and strain:1.35%) where SV-MoS ₂ shows the low overpotential with enhanced HER performance.	25
Figure 1.13:	(a) Schematic representation of the solvothermal synthesis of MoS ₂ /rGO hybrid; (b) polarization and Tafel curve obtained from rGO, MoS ₂ NP, and MoS ₂ /rGO catalysts, respectively; (c) HER scheme for MoS _x /NCNT forest hybrid catalyst and corresponding polarization curve.	28
Figure 1.14:	(a) The relation between current ($\log(i_0)$) vs. ΔG_H^0 presents a Volcano curve, the inset graph point to a different configuration of the doped MoS ₂ as coordinated with four and six S atoms. The adoption sites for H the atoms are represented by red dashed circles. The studied metal atoms are located in the periodic table, as shown by the inset at the bottom. Green, yellow, blue, and purple represents the Mo, S, and doped metal atoms. (b) The results of the DFT calculation and the corresponding electrocatalytic on the surface of different catalysts under the alkaline medium. $\Delta G(H_2O)$ and $\Delta G(H)$ are related to the kinetics energy barriers for the Volcano and Tafel steps on the catalysts, respectively, and $\Delta G(OH)$ is the Gibbs free energy of the adsorbed OH ⁻ on the surface of the catalysts. In the diagram E (eV) represent the free energies of the different reactive stages. S, Mo, and Ni, are represented in yellow, blue, and red spheres. (c) shows the structural modal of oxygen incorporated MoS ₂ with large d-spacing (9.5 Å) compared to the pristine MoS ₂ (6.15 Å) (d) (left) calculated DOS of the oxygen incorporated MoS ₂ (top) and the pristine MoS ₂ (bottom), the orange shading indicates the bandgap of pristine MoS ₂ decreased after the oxygen incorporation, (right) the charge density distribution of valance band and conduction band near the oxygen atom in the oxygen incorporated MoS ₂	31

	nanosheets, respectively. Contour line of the charge density represented by black line. (c) (left) HER free energy diagram for P and S site in the basal plane of pristine MoS ₂ and P-doped MoS ₂ . Insets show that the P-doped MoS ₂ with ' <i>H_{ad}</i> ' atom on the most active sites of the P site, (right) shows that the calculated free energy diagram for HER on P-doped MoS ₂ with different interlayer spacing values measured by the experimental process (0.65 nm and 0.91 nm).	
Figure 1.15:	(a) Semiconducting 2H-MoS ₂ to metallic 1T-MoS ₂ phase conversion by lithium intercalation and exfoliation; (b) shows the corresponding polarization curve where 1T MoS ₂ exhibits the high HER catalytic activity compared to the semiconducting 2H MoS ₂ ; (c) (right) crystal structure of 2H MoS ₂ ; (left) schematic of the battery testing system. The cathode is a MoS ₂ nanofilm with molecular layers perpendicular to the substrate, where the yellow and green colours represent the terrace sites and edge sites, respectively. The Li foil was used as the anode. (d) The Galvanostatic discharge curve shows the lithiation process; Li intercalates into the van der Waals gaps of 2H MoS ₂ to donate electrons to the slabs and expand the layer spacing of MoS ₂ . The voltage monotonically drops to 1.2 V vs. Li ⁺ /Li to reach a Li content of 0.28 V, after which the system undergoes a semiconducting 2H MoS ₂ to metallic 1T MoS ₂ phase transition. The atomic structure is changed from trigonal prismatic to octahedral.	34
Figure 1.16:	Shows (a–c) SEM images depicting morphologies of MoNi ₄ /MoO ₂ @Ni; (d–f) HRTEM images of MoNi ₄ /MoO ₂ @Ni and the inset of (d) shows the selected area electron diffraction (SAED) image; (g) TEM-EDS elemental mapping images of the MoNi ₄ electrocatalyst and the MoO ₂ cuboids. [scale bars, (a) 20 μm; (b) 1 μm; (c) 100 nm; (d–f) 2 nm; inset in d, 1 1/nm; (g) 20 nm].	37
Figure 2.1:	Shows (a) Autoclave used for hydrothermal synthesis; (b) laboratory vacuum oven, and (c) atmospheric controlled laboratory tube furnace, which were used for all the synthesis processes for this work.	61
Figure 2.2:	Schematic of the MoNi ₄ /MoO ₂ nanorod synthesized by a one-pot hydrothermal process.	62
Figure 2.3:	Step-by-Step Synthesis of Graphene oxide (GO); and reduced graphene oxide (rGO) by using the modified Hummers' method.	63
Figure 2.4:	Shows the transmission electron micrographs of graphene oxide (GO), and reduced graphene oxide (rGO) by using the modified Hummers' method followed by microwave heat treatment.	64

Figure 2.5:	Schematic showing the step-by-step synthesis of MoNi ₄ /MoO ₂ :rGO nanocomposite.	65
Figure 2.6:	Schematic of the 2D-MoS ₂ synthesized by a one-pot hydrothermal process.	66
Figure 2.7:	Schematic of the step-by-step synthesis of MoS ₂ :MoNi ₄ /MoO ₂ .	67
Figure 2.8:	Schematic showing the step-by-step synthesis of MoS ₂ and functionalized MoS ₂ nanosheets.	68
Figure 2.9:	Schematic showing the step-by-step synthesis of SO ₃ H/SO ₃ functionalized MoS ₂ nanosheets.	69
Figure 2.10:	Shows the pictographic image of Rigaku (miniflex 600) X-ray Diffractometer.	70
Figure 2.11:	The field emission scanning electron microscope (Nova Nano SEM 450, FEI) equipped with the energy-dispersive spectrometer (EDS) mostly used for this research work	71
Figure 2.12:	Shows a transmission electron microscope (TECNAI G2 20 TWIN, FEI-USA) equipped with the energy-dispersive X-ray spectroscopy (EDX) used for analyzing nanostructures for this research work.	72
Figure 2.13:	Shows the instrument for analysing X-ray photoelectron spectroscopy (XPS) (K-alpha, XPS dispersive spectrometer, Thermo Scientific).	73
Figure 2.14:	Confocal Raman microscopy system (UHTS α -300, WITec GmbH, Germany) in-built with a 532 nm laser source.	74
Figure 2.15:	FTIR spectrophotometer (THERMO Electron Scientific, Instruments LLC, Model No: Nicolet iS5 instrument) used for all the FTIR measurements.	75
Figure 2.16:	(a) Shows pictographic images of (a) Thermogravimetric analysis (TGA-50, M/s Shimadzu Pte Ltd.) and (b) Differential scanning calorimetry (DSC-60 Plus, M/s Shimadzu Pte Ltd.) instrument.	75
Figure 2.17:	UV-Visible spectrophotometer (Model No: V-770, JASCO, Japan) used for all the UV-Vis measurements for this work.	76
Figure 2.18:	Autosorb IQ2 BET instrument for the surface area measurement.	77
Figure 2.19:	Optical tensiometer instrument for contact angle measurements.	77

Figure 2.20:	(a) Shows the step-by-step process for working electrode fabrication; (b) working electrode (WE) after the drop casting on 1 cm ² graphite paper.	78
Figure 2.21:	Schematic representation of a three-electrode system for electrochemical measurements. In this scheme, graphite and Ag/AgCl is used as a counter and reference electrode, respectively; and as-synthesized electrocatalytic electrodes on graphite paper/Ni foam were used as the working electrode for all the experiments.	79
Figure 2.22:	(a) Different electrolytes used during the electrochemical measurements; (b) Ar gas purging of any of the standard electrolyte solutions before using it for electrochemical measurements; (c) represents the photographic images of different electrodes (such as WE, CE, RE) used for all these electrochemical measurements; (d) three-electrode arrangements for different electrochemical measurements; (e) AMETEK (PARSTAT 1000/2000A MC) dual-channel electrochemical workstation, where all the electrochemical measurements were performed.	80
Figure 3.1:	Shows (a) X-ray diffraction (XRD) pattern; (b) Raman spectra of rGO, MoNi ₄ /MoO ₂ , and MoNi ₄ /MoO ₂ :rGO nanocomposite.	89
Figure 3.2:	Shows the transmission electron micrographs (TEM) of (a and b) MoNi ₄ /MoO ₂ nanorods where MoNi ₄ nanocrystals are grown on MoO ₂ nanorods (black dots); (c) high-resolution transmission electron micrographs (HRTEM) and (d) SAED pattern of MoNi ₄ /MoO ₂ .	90
Figure 3.3:	Shows the transmission electron micrographs (TEM) of (a & b) MoNi ₄ /MoO ₂ nanorods where MoNi ₄ nanocrystals are grown on MoO ₂ nanorods; (c) high-resolution transmission electron micrographs (HRTEM) and; (d) SAED pattern of MoNi ₄ /MoO ₂ .	91
Figure 3.4:	Illustrates (a) Transmission electron micrograph and (b) SAED pattern of graphene oxide (GO); (c) Transmission electron micrograph (TEM) and (d) SAED of reduced graphene oxide (rGO).	92
Figure 3.5:	Shows the transmission electron micrographs (TEM) of (a, b and c) MoNi ₄ /MoO ₂ :rGO nanocomposite where MoNi ₄ nanocrystals are grown on MoO ₂ nanorods are supported by rGO sheets (d) SAED pattern of MoNi ₄ /MoO ₂ :rGO nanocomposite.	93
Figure 3.6:	(a) Polarization curve for HER on Ni foam (1×1cm ²) area; (b) corresponding overpotential (η_{10}); (c) Tafel plots for the various catalysts derived from the LSV; (d) EIS Nyquist plot; (e) corresponding charge transfer resistance (R_{ct}), and (f)	97

	Chronoamperometric (j-t) response for MoNi ₄ /MoO ₂ :rGO nanocomposite at a constant overpotential of 200 mV.	
Figure 4.1:	Shows (a) Comparative XRD patterns of 2D MoS ₂ , MoNi ₄ /MoO ₂ nanorod, and MoS ₂ :MoNi ₄ /MoO ₂ nanohybrids; (b) XRD patterns of MoNi ₄ /MoO ₂ .	109
Figure 4.2:	Shows the FESEM images of (a) MoNi ₄ /MoO ₂ nanorods; (b) MoNi ₄ nanocrystals grown on MoO ₂ nanorods; (c) a few as-grown nanohybrids of MoS ₂ :MoNi ₄ /MoO ₂ showing homogeneous coating of MoS ₂ on MoNi ₄ /MoO ₂ ; (d) & (e) illustrate the nanohybrids with homogeneous coating, large surface area, vertically oriented 2D flake-like of MoS ₂ grown on MoNi ₄ /MoO ₂ nanorods with flake size of ~ 300-500 nm; (f) vertical 2D MoS ₂ flakes with a thickness of ~ 2-5 nm with sharp edges, which helps in faster electronic transfer, thus, improve the catalytic activity of the nanocomposite.	110
Figure 4.3:	Energy dispersive spectroscopy of MoNi ₄ /MoO ₂ nanorods recorded during SEM.	112
Figure 4.4:	(a, b) Bright field transmission electron micrographs of MoNi ₄ /MoO ₂ nanohybrid with different morphologies; (c) SAED pattern of characteristic MoNi ₄ /MoO ₂ planes; (d, e, g, h) As-grown 2D MoS ₂ on MoNi ₄ /MoO ₂ nanorods with flaky entangled morphologies; (f) SAED pattern of characteristic MoS ₂ :MoNi ₄ /MoO ₂ ; (i) High-resolution transmission electron micrograph of layered MoS ₂ with the (002) plane.	113
Figure 4.5:	Shows (a) a TEM image of a two-dimensional MoS ₂ coated: MoNi ₄ /MoO ₂ nanohybrid; (b) illustrates the scanning transmission electron microscopy images of a similar structure with clearly visible flaky 2D MoS ₂ coated onto the transition-metal alloy nanorod.	115
Figure 4.6:	(a) Shows the STEM image of a MoS ₂ :MoNi ₄ /MoO ₂ nanohybrid; (b) illustrates the EDS mapping of the nanohybrid showing comprehensive elemental mapping; (c-f) shows the various elemental distributions obtained in EDS mapping, such as, (c) Molybdenum, (d) Sulfur, (e) Nickel, and (f) Oxygen.	116
Figure 4.7:	Schematic demonstrating step-by-step mechanism of the growth of 2D MoS ₂ on the MoNi ₄ /MoO ₂ nanorod.	117
Figure 4.8:	Shows the comparative (a) Mo 3d peaks; (b) Ni 2p peaks obtained from X-ray photoelectron spectroscopy of MoNi ₄ /MoO ₂ ; and MoS ₂ :MoNi ₄ /MoO ₂ hybrid; (c) and (d) illustrate O 1s peak from MoNi ₄ /MoO ₂ sample and S 2p peak from the hybrid sample; respectively.	119
Figure 4.9:	Illustrates (a) the comparative LSV plot of current density versus	121

	potential curve showing the onset potential for the hydrogen generation for all samples; (b) the correlative Tafel slopes for all samples; (c) the stability test of as-grown hybrid MoS ₂ :MoNi ₄ /MoO ₂ electrocatalysts at constant overpotential at 200 mV; (d) A comparable linear sweep voltammetry (LSV) plot depicting the performance of the hybrid electrode before and after the stability test.	
Figure 4.10:	(a-c) Shows the cyclic voltammetry (CV) with different scan rates of 20-100 mV/s for MoNi ₄ /MoO ₂ nanorod, MoS ₂ , and MoS ₂ :MoNi ₄ /MoO ₂ nanohybrids. (d) Comparative C _d plot as a function of scan rate	124
Figure 4.11:	Comparative cyclic voltammetry curves of MoNi ₄ /MoO ₂ , MoS ₂ , and MoS ₂ :MoNi ₄ /MoO ₂ hybrid structure recorded between -0.6 V to 0.6 V vs. RHE in 1M KOH at a scan rate of 20 mV/s.	125
Figure 4.12:	Comparable EIS data for pristine MoS ₂ , MoNi ₄ /MoO ₂ , and MoS ₂ :MoNi ₄ /MoO ₂ hybrid sample.	127
Figure 5.1:	Comparative Raman Spectra of all as-synthesized MoS ₂ samples with the different molar ratios of thiourea	143
Figure 5.2:	Shows (a) comparative Fourier transform infrared (FTIR) spectra of all pristine and functionalized MoS ₂ sample; (b) A comparative FTIR spectra of MoS ₂ -8 and MoS ₂ -10.	144
Figure 5.3:	High-resolution Mo 3d XPS spectrum of all as-synthesized MoS ₂ nanosheets with varying molar ratios of thiourea. The entire XPS spectrum was analyzed by the CasaXPS software. The two characteristic peaks Mo 3d _{5/2} and Mo 3d _{3/2} located at ~229.17±0.28 eV and ~232.32±0.28 eV correspond to the Mo ⁴⁺ oxidation states, while the peak located at ~226.40±0.25 eV to S 2s in MoS ₂ .	145
Figure 5.4:	(a ₁ -e ₁) Comparative S 2p; and (a ₂ -e ₂) O 1s peak obtained from X-ray photoelectron spectroscopy of as-synthesized MoS ₂ nanosheets with varying molar ratios of thiourea.	147
Figure 5.5:	Shows a comparative XRD plots of all as-synthesized MoS ₂ nanosheets with varying molar ratios of thiourea compared with MoS ₂ (JCPDS # 98-001-8125).	150
Figure 5.6:	Shows the scanning electron micrographs with different magnifications with scale bars of ~500 nm and ~200 nm, (a ₁ and a ₂) MoS ₂ -2, (b ₁ and b ₂) MoS ₂ -4, (c ₁ and c ₂) MoS ₂ -6, (d ₁ and d ₂) MoS ₂ -8 and (e ₁ and e ₂) MoS ₂ -10.	151
Figure 5.7:	Figure 5.7: (a ₁ , a ₂ , a ₃ , and a ₄) Shows the TEM, SAED pattern, and HRTEM of MoS ₂ -2 with the interlayer d-spacing of 6.1 Å; (b ₁ , b ₂ , b ₃ , and b ₄) TEM, SAED pattern, and HRTEM of MoS ₂ -4 with the interlayer d-spacing of 6.3 Å; (c ₁ , c ₂ , c ₃ , and c ₄) TEM, SAED	152

	pattern and HRTEM of MoS ₂ -6 with the interlayer d-spacing of 9.4 Å; (d ₁ , d ₂ , d ₃ , and d ₄) TEM, SAED pattern and HRTEM of MoS ₂ -8 with the interlayer d-spacing of 9.4 Å; and (e ₁ , e ₂ , e ₃ , and e ₄) TEM, SAED pattern and HRTEM of MoS ₂ -10 with the interlayer d-spacing of 9.4 Å.	
Figure 5.8:	Shows (a) the TGA and DSC curves for MoS ₂ -8; (b) shows the XRD pattern of MoS ₂ -8 before and after the annealing at 350 °C for 2h in an inert gas atmosphere.	154
Figure 5.9:	Shows (a) TEM, (b) SAED pattern; (c & d) HETRM of MoS ₂ -8 sample after annealing at 350 °C for 2h in an inert gas atmosphere; (f) the IFFT line profile of MoS ₂ -8 after annealing with the interlayer d-spacing 6.28 Å.	155
Figure 5.10:	Demonstrates contact angle images of a water droplet on as-synthesised (a) MoS ₂ -2; (b) MoS ₂ -4; (c) sulfonic acid (-SO ₃ H) group functionalized MoS ₂ (MoS ₂ -8); (d) a comparative contact angle data of MoS ₂ -2 (69°), MoS ₂ -4 (106°), and (MoS ₂ -8 (38°); (e) represents the time dependent dynamic contact angle measurement data showing the lowering of contact angle for MoS ₂ -8, depicting the improvement in hydrophilicity of the sample.	156
Figure 5.11:	Comparative Mott-Schottky plot of all as-synthesized MoS ₂ nanosheets with varying molar ratios of thiourea.	157
Figure 5.12:	Shows (a) Polarization curve of as-synthesized MoS ₂ nanosheets; (b) the corresponding comparative Tafel plot; (c) Nyquist plots; and (d) the stability of the electrode prepared using MoS ₂ -8 sample.	159
Figure 5.13:	(a-e) Show the cyclic voltammetry (CV) with different scan rates of 20-100 mV/s for MoS ₂ -2 to MoS ₂ -10; (f) Comparative C _{dl} plot as a function of scan rate.	163
Figure 5.14:	Shows comparative XPS spectra of before and after the 12h stability data of MoS ₂ -8 samples depicting (a ₁ -a ₂) Mo3d, (b ₁ .b ₂) S 2p, and (c ₁ -c ₂) O1s.	164
Figure 5.15:	Comparative Raman spectra of the same electrode taken before and after the stability test showing the characteristics of MoS ₂ peaks at the corresponding position ~ 369.7 cm ⁻¹ (E _{2g} ¹) and 398.5 cm ⁻¹ (A _{1g}) before the stability test while the same position was found at ~ 372.2 cm ⁻¹ (E _{2g} ¹) and 398.5 cm ⁻¹ (A _{1g}) for the electrode after the stability test. In this regard, it should be mentioned that even after the stability test for 12h in 1M KOH solution at 10 mA/cm current density, no significant changes in the bonding and structure were observed for the as-functionalized 2D-MoS ₂ nanosheets (MoS ₂ -8) catalyst.	164

Figure 5.16:	Shows comparative XPS spectra of before and after the 12h stability data of MoS ₂ -8 samples depicting (a ₁ -a ₂) Mo3d, (b ₁ .b ₂) S 2p, and (c ₁ -c ₂) O1s.	165
Figure 5.17:	(a) & (b) Show the respective side view and top view of the optimized structure of the MoS ₂ -SO ₃ H surface. (c) & (d) shows the side view and top view of the differential charge density plots calculated for the MoS ₂ -SO ₃ H surface. The isosurface level is 0.06 e/Å ³ (e) total density of states of the pristine and SO ₃ H functionalized surface and (f) The orbital resolved partial density of states of the MoS ₂ +SO ₃ H surface.	168
Figure 5.18:	(a) Band-structure of the MoS ₂ surface; (b) Band-structure of the MoS ₂ +SO ₃ H surface; (c) Vacuum potential calculated for the MoS ₂ surface; (d) Vacuum potential of the MoS ₂ +SO ₃ H surface.	169
Figure 6.1:	Shows (a) Fourier transform infrared (FTIR) spectrum of SO ₃ H/SO ₃ -MoS ₂ ; (b) Raman spectra of the SO ₃ H/SO ₃ -MoS ₂ nanosheets; (c) & (d) high-resolution S 2p XPS spectrum and O1s XPS spectrum, respectively.	188
Figure 6.2:	Figure 6.2: XRD diffraction pattern of as-synthesized MoS ₂ (Pristine MoS ₂) with the interlayer spacing (d) of 6.3 Å and SO ₃ H/SO ₃ -MoS ₂ with the interlayer spacing (d) of 9.4 Å.	189
Figure 6.3:	Shows (a) SEM images demonstrating morphology of SO ₃ H/SO ₃ functionalized MoS ₂ nanosheets; (b) the bright-field transmission electron micrograph of as-synthesized SO ₃ H/SO ₃ -MoS ₂ ; (c) electron diffraction pattern; (d) & (e) illustrate HRTEM depicting the interlayer d-spacing of functionalized 2D-MoS ₂ ; (f) line intensity profile of the line drawn in the inverse FFT image.	190
Figure 6.4:	Shows (a) Transmission electron micrograph of pristine 2D-MoS ₂ (i.e., P-MoS ₂); (b) SAED pattern of pristine 2D-MoS ₂ depicts characteristics crystal planes of (110), (013), and (010); (c) the HRTEM images of typical few-layered 2D-MoS ₂ with an interplanar distance of 6.3 Å; (d) line intensity profile of the line drawn in the inverse FFT image (GATAN Inc., USA).	191
Figure. 6.5:	Shows (a) UV-Vis absorbance spectra of SO ₃ H/SO ₃ -MoS ₂ as a function of time in 10 ppm MB dye solution; (b) the representative photographic images were taken for studying the comparative photocatalytic activity of SO ₃ H/SO ₃ -MoS ₂ as a function of time for 10 ppm solution; (c) and (d) illustrates UV-Vis absorbance spectra of SO ₃ H/SO ₃ -MoS ₂ at 5 ppm & 15 ppm MB dye solutions.	193
Figure 6.6:	UV-Vis absorbance spectra as a function of time of (a) B-MoS ₂ ; and (b) P-MoS ₂ in 10 ppm MB dye.	194

Figure 6.7:	Shows (a) the comparative normalized intensity as a function of time illustrating the rate of MB dye degradation at 5, 10 & 15 ppm solution; (b) comparative normalized intensity plots for SO ₃ H/SO ₃ -MoS ₂ , P-MoS ₂ , B-MoS ₂ and as a function of time illustrating the MB dye degradation rate in 10 ppm dye solution; (c) the comparative rate kinetics plots of photocatalytic dye degradation reactions using the 10 ppm dye solution using SO ₃ H/SO ₃ -MoS ₂ ; (d) demonstrates the rate kinetics plot of photocatalytic MB degradation using SO ₃ H/ SO ₃ -MoS ₂ , P-MoS ₂ , and B-MoS ₂ .	195
Figure 6.8:	(a) Illustrates (a) the comparative N ₂ adsorption/desorption isotherms data of SO ₃ H/SO ₃ -MoS ₂ and P-MoS ₂ obtained during the BET measurement; (b) shows the comparative Tauc plot of P-MoS ₂ and SO ₃ H/SO ₃ -MoS ₂ .	197
Figure 6.9:	Schematic illustrating the mechanism of dye degradation using functionalized-MoS ₂ samples.	198

LIST OF TABLES	
Table 3.1: Lists the electrochemical parameters of various electrocatalysts samples of MoNi ₄ /MoO ₂ , rGO, and MoNi ₄ /MoO ₂ :rGO nanocomposite.	98
Table 4.1: Lists the comparative electrochemical performances of MoS ₂ , MoNi ₄ /MoO ₂ and MoS ₂ :MoNi ₄ /MoO ₂ nanohybrids electrocatalysts	122
Table 4.2: Lists the fitting parameters from the EIS equivalent circuit model	128
Table 4.3: The comparative HER performances of MoS ₂ :MoNi ₄ /MoO ₂ nanohybrid with various other MoS ₂ -based hybrid electrocatalysts reported to date.	128
Table 5.1: Lists the Raman peak positions of various MoS ₂ samples	143
Table 5.2: Demonstrates XPS peak parameters for all MoS ₂ samples	148
Table 5.3: Calculated flat band potential (E_{FB}) of as-synthesised pristine and functionalized MoS ₂	157
Table 5.4: Lists HER performances of all MoS ₂ electrocatalyst in 1M KOH solution	160
Table 5.5: EIS fitting parameters from the equivalent circuit model for all the samples	162
Table 5.6: The Bader charges calculated for the MoS ₂ -SO ₃ H surface, for the atoms directly below the -SO ₃ H attachment	167

LIST OF ABBREVIATIONS

Abbreviation	Details
XRD	X-ray powder diffraction
FESEM	Field-emission scanning electron microscopy
TEM	Transmission electron microscopy
HRTEM	High-resolution transmission electron microscopy
XPS	X-ray photoemission spectroscopy
FTIR	Fourier transform infrared spectroscopy
UV-Vis	Ultraviolet-visible spectroscopy
TGA	Thermogravimetric analysis
DSC	Differential scanning calorimetry
BET	Brunauer-Emmett-Teller
SAED	Selected area electron diffraction
EDS	Energy dispersive spectroscopy
STEM	Scanning transmission electron microscopy
LSV	Linear sweep voltammetry
EIS	Electrochemical impedance spectroscopy
CV	Cyclic voltammetry
ECSA	Electrochemical surface area
M-S	Mott-Schottky
EWS	Electrochemical water splitting
HER	Hydrogen evolution reaction

CE	Counter electrode
WE	Working electrode
RE	Reference electrode
RHE	Reversible hydrogen electrode
KOH	Potassium hydroxide
KCl	Potassium chloride
GP	Graphite paper
AgCl	Silver chloride
CFP	Carbon fiber paper
HTS	Hydrothermal synthesis
CPE	Constant phase element
MoO ₂	Molybdenum dioxide
GO	Graphene oxide
rGO	Reduced graphene oxide
H ₂ SO ₄	Sulfuric acid
H ₃ PO ₄	Phosphoric acid
KMnO ₄	Potassium permanganate
DI water	Deionized water
H ₂ O ₂	Hydrogen peroxide
RT	Room temperature
2D	Two dimensional
1D	One dimensional
3D	Three dimensional
NP	Nanoplates

MoS ₃	Molybdenum trisulfide
MoS ₂	Molybdenum disulfide
SO ₃ H	Sulfonic acid
SO ₃	Sulfur trioxide
TMDs	Transition metal dichalcogenides
CNT	Carbon nanotube
DFT	Density Functional Theory
IFFT	Inverse Fast Fourier Transition
DOS	Density of states
VBM	Valence band maximum
CBM	Conduction band minimum
WF	Work function
VASP	Vienna Ab initio Simulation Package
GGA	Generalized gradient approximation
PBE	Perdew–Burke–Ernzerhof
MB	Methylene blue
LED	Light-emitting diode
B-MoS ₂	Bulk molybdenum disulfide
P-MoS ₂	Pristine molybdenum disulfide